Nano Research
2023, 16(10): 12043–12049
ISSN 1998-0124 CN 11-5974/O4
https://doi.org/10.1007/s12274-022-5079-7

Research Article

Ni_3B modified $BiVO_4$ photoanodes for enhanced photoelectrochemical water splitting: The key role of Ni_3B on reducing the water oxidation barrier

Kehui Xue[1,§], Haifeng Zhu[2,§], Xingyu Zhao[1], Liana Alvares Rodrigues[3], D. Amaranatha Reddy[4], Yaping Zhang[2], and Lianqing Yu[1] (✉)

[1] School of Materials Science and Engineering, China University of Petroleum (East China), QingDao 266580, China
[2] College of Science, China University of Petroleum (East China), QingDao 266580, China
[3] Engineering School of Lorena, University of São Paulo, CEP 12602-810, São Paulo, Brazil
[4] Indian Institute of Information Technology Design and Manufacturing, Kurnool 518007, India
[§] Kehui Xue and Haifeng Zhu contributed equally to this work.

Received: 6 July 2022 / **Revised:** 22 August 2022 / **Accepted:** 20 September 2022

ABSTRACT

Bismuth vanadate ($BiVO_4$, BVO) as a promising photoelectrode has been received great attention for photoelectrochemical (PEC) water splitting. However, the slow oxidation kinetics on the surface of $BiVO_4$ limited the PEC water splitting efficiency. Herein, nickel boride (Ni_3B, NB) nanoparticles, generally used in electrocatalytic field material, were modified on the surface of $BiVO_4$ photoelectrode as an efficient cocatalyst to accelerate the oxygen evolution reaction. The as-prepared BVO-NB-5P photoelectrode exhibits a remarkable photocurrent density of 1.47 mA·cm^{-2} at 1.23 V versus the reversible hydrogen electrode (RHE) under air mass (AM) 1.5 G illumination, which is about 2.8 times higher than the bare $BiVO_4$ photoelectrode, and its water splitting rate is 11.3 times higher than bare $BiVO_4$. The PEC studies reveal that the spin coated Ni_3B crystal cocatalyst could effectively reduce the water oxidation barrier, and improve the surface charge injection efficiency to 94%, which could boost the photogenerated holes reaction to enhance the PEC performance of $BiVO_4$ photoelectrode.

KEYWORDS

photoelectrochemical, water splitting, $BiVO_4$, Ni_3B

1 Introduction

As a clean and renewable energy carrier, hydrogen is regarded as the most effective way to resolve the energy and environmental crisis [1, 2]. However, H_2 is produced industrially by separation from fossil fuels, which is accompanied by CO_2 production and the deterioration of environment [3]. Direct splitting of water to H_2 by solar energy is regarded as an ideal method [4, 5]. In 1972, Fujishima et al. [6] first reported the photoelectrochemical (PEC) system consisting of TiO_2 electrode and Pt electrode, and found that TiO_2 photocatalyst could produce H_2. The reduction and oxidation process in the PEC system occurred at two electrodes, which means that the H_2 and O_2 can be effectively separated [7, 8]. Another advantage of the system is that the catalyst can be easily removed from the water.

Bismuth vanadate ($BiVO_4$, BVO) is an n-type semiconductor with a narrow bandgap (2.4 eV) [9], and its conduction band (CB) edge is slightly lower than the redox potential of H^+/H_2. $BiVO_4$ photoanode material can absorb 11% energy of the solar spectrum [10], resulting in a high theoretical photocurrent density of 7.6 mA·cm^{-2} and solar-to-hydrogen conversion efficiency of 9.3% [11, 12]. However, the actual energy conversion efficiency is less than the theoretical value because of low electron transfer capacity [13], slow oxidation kinetic rate [14], and poor photocarrier mobility [15]. Constructing heterojunctions such as $TiO_2/BiVO_4$ [16], $Cu_2O/BiVO_4$ [17], and $WO_3/BiVO_4$ [18] can accelerate charge separation and improve the PEC performance of $BiVO_4$, however, the slow kinetics of the oxygen evolution reaction (OER) still limits the solar energy conversion efficiency.

Modification $BiVO_4$ with water oxidation cocatalyst can be one of promising approaches to improve water oxidation kinetics, which can efficiently attract the holes from $BiVO_4$ to the interfaces of electrolyte/photoanode, and offer active sites for OER to reduce the overpotential [19]. Kang et al. [20] demonstrated that the $BiVO_4$ photoanode co-modified with borate and iron hydroxide exhibited high properties in PEC water oxidation, yielding a photocurrent value of 4.96 mA·cm^{-2}. The electron-deficient boron atom allows it to have a rich bonding chain model after combined with metals [21, 22]. The rich composition and structure in transition metal borides exhibit favorable application in catalytic water splitting. Among them, a cheap and efficient Ni_3B (NB) cocatalyst has shown high conductivity and OER rate on electrocatalytic field [23]. For example, Arivu et al. [24] synthesized a Ni_3B-reduced graphene oxide (rGO) composite and drop-casted onto a carbon fiber paper as free-standing anode, achieving 10 mA·cm^{-2} at an overpotential of 320 mV. Wu et al.

Address correspondence to iyy2000@163.com

[25] successfully synthesized an urchin-like Ni_3S_2@Ni_3B composite catalyst that showed outstanding catalytic performance for both OER and hydrogen evolution reaction (HER), achieving values of 1,000 mA·cm^{-2} at relatively low overpotentials of 517 and 632 mV, respectively. In a word, Ni_3B plays an important role on reducing the water oxidation barrier and optimizing the water-splitting reaction dynamics. So, what will happen if Ni_3B is utilized in photoelectrochemical research?

In this article, we implanted inexpensive electrocatalyst Ni_3B nanoparticles onto $BiVO_4$ electrode through a simple spin coating method. Compared to pure $BiVO_4$ photoanode, the composite photoanode exhibits much higher photoelectrochemical properties and water splitting performance, which could be attributed to the strong oxygen evolution capacity of the Ni_3B cocatalyst. In addition, a variety of characterization measures were performed to analyze the morphologies and structures of as-obtained samples. This work provides a non-noble metal cocatalyst in photoelectrochemical water splitting.

2 Experimental

2.1 Materials

All chemical reagents were purchased from Aladdin Reagent Co., Ltd., China. All the reagents employed in this study were of analytical grade and used without further purification.

2.2 Preparation $BiVO_4$ electrodes

First, 0.4 M $Bi(NO_3)_3$·$5H_2O$ was dissolved in 0.4 M KI solution (50 mL), and HNO_3 was added to adjust its pH value to 1.7. Subsequently, this solution was mixed with ethanol (20 mL) containing 0.23 M p-benzoquinone to acquire an electrodeposited solution. A typical three-electrode cell was used for electrodeposition, fluorine-doped tin oxide (FTO) as working electrode (WE), Ag/AgCl (4 M KCl) as reference electrode (RE), and platinum foil as counter electrode (CE), respectively. The electrodeposition was carried out at the potential of −0.1 V vs. Ag/AgCl for 3 min at room temperature to obtain the BiOI electrode. And then the BiOI on FTO electrode was covered with 0.2 M $VO(acac)_2$ dimethyl sulfoxide solution, and heated in the air at 450 °C for 2 h (the heating rate at 2 °C·min^{-1}) to convert BiOI to $BiVO_4$. After calcination, the electrode was impregnated into 1 M NaOH solution to remove excess V_2O_5. Finally, the pure $BiVO_4$ electrode was rinsed with deionized water and dried.

2.3 Synthesis of Ni_3B catalysts

5 mmol $Ni(ac)_2$·$4H_2O$ was dissolved in 50 mL deionized water under continuous stir. 10 mL of aqueous solution containing 1 M $NaBH_4$ and 0.1 M NaOH was added to the above solution. The mixed solution was kept agitating for 10 min. The products were collected by centrifugation and washed with deoxygenating deionized water and ethanol, then dried overnight in a vacuum furnace at 60 °C to obtain amorphous nickel boride (a-Ni_3B). Finally, the products were annealed in a tube furnace at 325 °C for 2 h to obtain Ni_3B.

2.4 Fabrication of $BiVO_4$/Ni_3B electrodes

1 mg a-Ni_3B nanoparticles were dispersed in 1 mL absolute ethanol and ultrasonicated for 30 min to form a uniform suspension. Subsequently, 20 μL of the suspension was spin-coated onto the $BiVO_4$ electrodes with 2,000 r·min^{-1} for 15 s. Finally, the photoelectrodes were annealed in Ar atmosphere at 325 °C for 2 h. The resulting photoelectrodes were named as BVO-NB-*x*, where *x* is 1, 3, 5, 7, and 9. The BVO-NB-5 photoelectrode without annealing was named as BVO-NB-5a. To further improve performance, the sample BVO-NB-5 was physically pressed with 20 N before annealing, which was named as BVO-NB-5P.

2.5 Characterizations

X-ray diffraction (XRD) was performed by DX-2700 X-ray diffractometer (Dandong Fangyuan, China) with monochromatized Cu-Kα radiation (λ = 1.5418 Å) at 40 kV and 30 mA. The morphology of the samples was investigated by scanning electron microscopy (SEM, TM4000, Hitachi Ltd., Japan) with energy dispersive X-ray spectroscopy (EDS). The transmission electron microscopy (TEM) (EM-2100) was used to obtain the lattice diffraction fringes and phases. Ultraviolet–visible (UV–vis) absorption spectra were recorded on a UV–vis spectrophotometer (HITACHI U-3900, Japan). Brunauer–Emmett–Teller (BET) specific surface area and Barrett–Joyner–Halenda (BJH) pore size distributions were obtained on N_2 adsorption–desorption isotherms at 77 K with an automatic gas adsorption analyzer (ASAP2460). Raman spectra (Horiba Scientific) were performed to study the phase structure of the samples. Photoluminescent (PL) spectra were collected on a F-7100 spectrofluorometer to estimate the recombination rate of the photo-induced electrons and holes for composites.

2.6 Photoelectrochemical measurements

The PEC measurements were carried out in a standard three-electrode configuration with the prepared photoelectrodes as working electrode, Ag/AgCl electrode as the reference electrode, and Pt wire as the counter electrode, respectively. The measurement was performed by a CHI 760E electrochemical workstation (Shanghai CH instrument Co., Ltd., China). A 300 W xenon lamp coupled with an AM 1.5 G filter was applied as the simulated sunlight source (100 mA·cm^{-2}). Linear sweep voltammetry (LSV), photocurrent-time, electrochemical impedance spectroscopy (EIS) in the frequency range of 10^{-2}–10^5 Hz, and Mott–Schottky tests were carried out in 0.1 M Na_2SO_4 (pH = 7) electrolyte solution. For all samples, the light was irradiated from the backside of the FTO substrate. The hole scavenger of Na_2SO_3 (0.1 M) was used for measuring the injection efficiency.

3 Results and discussion

Crystal structures of the catalysts were investigated by using XRD. The XRD pattern of a broad peak indicates the amorphous structure of a-Ni_3B (Fig. 1(a)). After annealing, all peaks can be assigned to Ni_3B (PDF#48-1223), clearly suggesting the appearance of Ni_3B. Figure 1(b) shows the XRD images of $BiVO_4$ and BVO-NB-5P photoelectrodes. It can be seen that pure $BiVO_4$ (PDF#83-1699) is successfully prepared. Compared to pure $BiVO_4$, the BVO-NB-5P photoelectrode do not show any other obvious diffraction peaks, and the peak intensity slightly decreases due to Ni_3B nanoparticles coverage. And cocatalyst Ni_3B cannot be detected in all samples because of its low content and well distribution, as exhibited in Fig. S1 in the Electronic Supplementary Material (ESM).

Figure 2 shows the SEM images of as-synthesized $BiVO_4$, Ni_3B, and BVO-NB-5P samples. From Fig. 2(a), the as-synthesized $BiVO_4$ exhibits a porous worm-like structure with diameter of about 300–600 nm, and is uniformly grown on FTO substrate. As shown in Fig. 2(b), pure Ni_3B displays relatively homogeneous nanoparticles. This small nanoparticle of Ni_3B is favorable to combine with $BiVO_4$ porous structure. After the spin coating and annealing process, the morphology of the BVO-NB-5P composite electrode is shown in Fig. 2(c). Obviously, after physically pressed 20 N, a tightly covered nanolayer of Ni_3B is formed on $BiVO_4$.

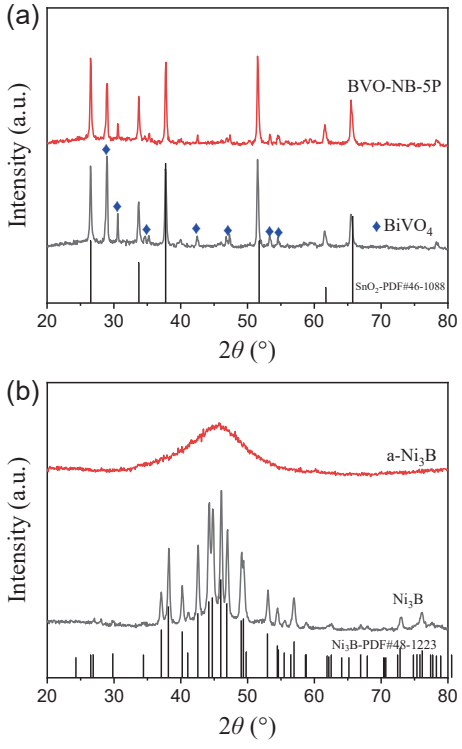

Figure 1 XRD patterns of (a) a-Ni_3B and annealed Ni_3B, and (b) $BiVO_4$ and BVO-NB-5P.

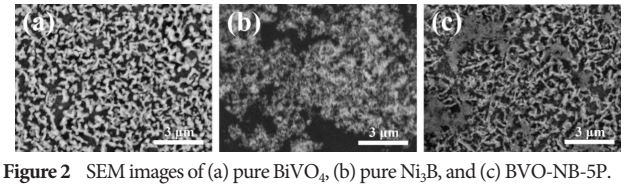

Figure 2 SEM images of (a) pure $BiVO_4$, (b) pure Ni_3B, and (c) BVO-NB-5P.

This interesting structure can facilitate the transport of carriers between interfaces and improve photoelectrochemical performance.

The element distribution and composition of BVO-Nb-5P were further confirmed, as shown in Fig. 3. Bi, V, and O elements coming from $BiVO_4$ substrate are evenly distributed. The signals of Ni element are concentrated at the position of Ni_3B. Because B is light element, the detection of B element in the elemental maps is not accurate. The atomic percentage in the EDS spectrum also confirms the well distribution of each element. The results indicate that the cocatalyst Ni_3B was successfully synthesized on the surface of $BiVO_4$ photoelectrode.

The TEM and high-resolution TEM (HRTEM) microstructures of samples were observed, as shown in Fig. 4. In TEM images (Figs. 4(a) and 4(b)), $BiVO_4$ photoelectrode shows clean and smooth surface and Ni_3B nanoparticles have a smaller size at about 5 nm. As presented in Fig. 4(c), after the coating of Ni_3B, a thin layer of Ni_3B nanoparticles is loaded on the crystal surface of $BiVO_4$ and Ni_3B nanoparticles are uniformly attached to the crystal surface of $BiVO_4$, leading to rough surface of BVO-NB-5P hybrid materials. This result is in accord with the SEM images (Fig. 3(c)). Moreover, after Ni_3B loading on the surface of $BiVO_4$, no significant agglomeration occurred and Ni_3B is distributed with particles of about 5 nm (the area surrounded by the yellow circle). This phenomenon indicates that the morphology and size of Ni_3B are well maintained during the construction of the composite system, which facilitates the role of Ni_3B on reducing barriers to water oxidation. In HRTEM image of Fig. 4(d), the crystal plane space of 0.308 and 0.474 nm is corresponding to the (121) and (110) crystal planes of monoclinic $BiVO_4$, respectively.

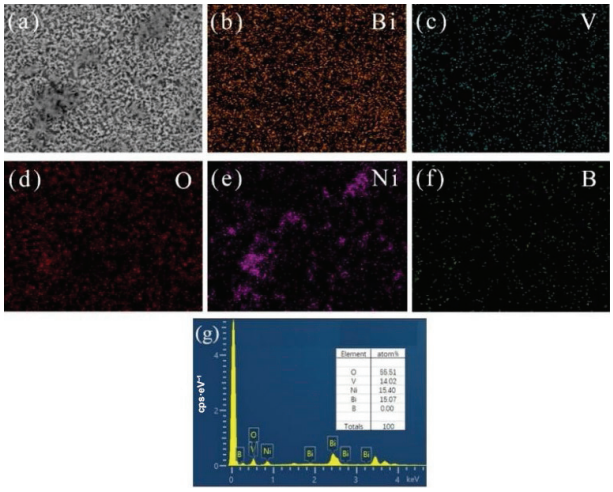

Figure 3 (a) SEM image of BVO-NB-5P and elemental maps of (b) Bi, (c) V, (d) O, (e) Ni, and (f) B. (g) EDS spectrum.

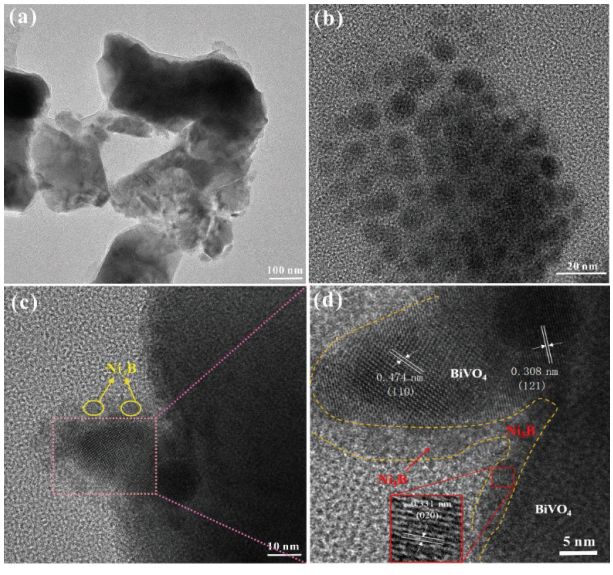

Figure 4 TEM images of (a) $BiVO_4$ and (b) Ni_3B. (c) and (d) HRTEM images of BVO-NB-5P.

Nanoparticles inside the yellow dot-line can be calibrated with 0.331 nm lattice space corresponding to the Ni_3B (020) crystal plane. This result proved that Ni_3B is evenly combined on the surface of $BiVO_4$. In addition, a close interface is formed between $BiVO_4$ and Ni_3B, which is beneficial for the charge transfer.

The N_2 adsorption–desorption isotherms for the $BiVO_4$ and BVO-NB-5P are presented in Fig. 5. The results illustrate that $BiVO_4$ and BVO-NB-5P exhibit the typical type-IV isotherms on the basis of the IUPAC classification of solid/vapor equilibrium isothermal lines. Accordingly, BVO-NB-5P shows a larger specific surface area (33.20 m^2/g in Fig. 5(b)) compared to $BiVO_4$ (29.49 m^2/g in Fig. 5(a)). Meanwhile, the pore distribution plot of BVO-NB-5P displays a wide pore size distribution on the range of 2–40 nm (Fig. 5(b1)).

Raman spectra were conducted to explain the phase structure of samples excited by a laser (632 nm) at room temperature. As exhibited in Fig. 6(a), the Raman bands located at 118, 209, 325, 365, and 830 cm^{-1} for $BiVO_4$ and BVO-NB-5P are representative vibrational modes of $BiVO_4$. In general, Raman spectroscopy is a local probe that is sensitive to the local structure. After coating the Ni_3B, Raman spectrum of the BVO-NB-5P composite becomes weaker, which may be due to the obscuration of the $BiVO_4$ Raman signal by Ni_3B.

Apparently, the PL intensity of the BVO-NB-5P sample is lower

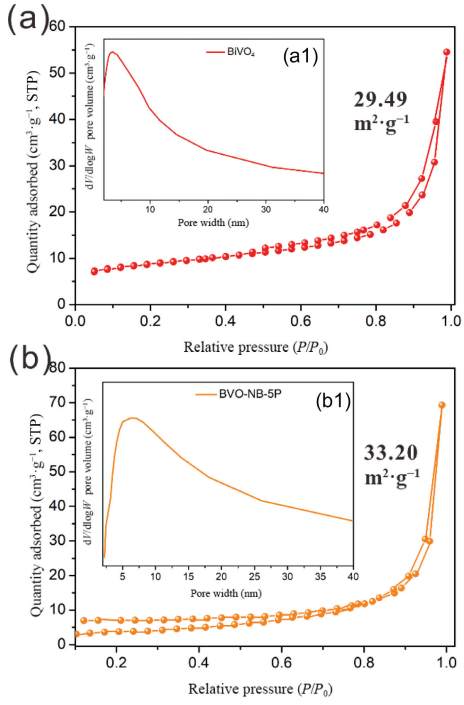

Figure 5 N_2 adsorption/desorption isotherms and corresponding pore size distributions of (a) $BiVO_4$ and (b) BVO-NB-5P.

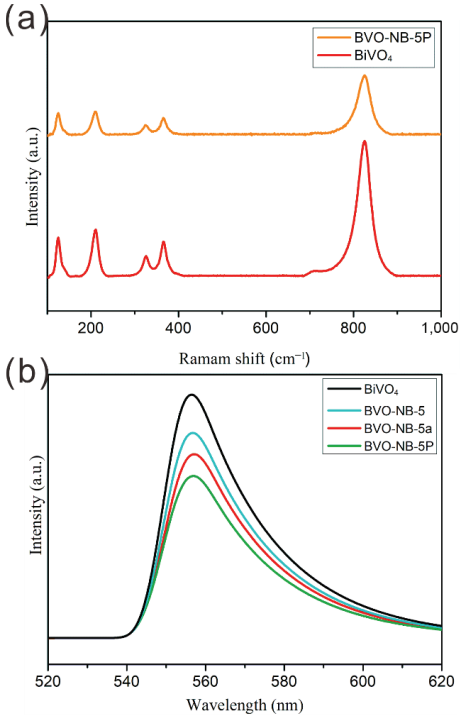

Figure 6 (a) Raman spectra of $BiVO_4$ and BVO-NB-5P. (b) PL spectra for samples.

than that of $BiVO_4$, BVO-NB-5, and BVO-NB-5a (Fig. 6(b)), which indicates that the composite system after the pressing treatment is favorable to suppress the recombination of photo-generated carriers and accelerate the transfer of electrons and holes. This further illustrates that the construction of a tight interface between $BiVO_4$ and Ni_3B can facilitate the charge transfer.

The UV–vis diffuse reflectance spectra were performed to further explore optical properties of samples. The results of $BiVO_4$, Ni_3B, and BVO-NB-5P are shown in Fig. 7(a). The $BiVO_4$ and BVO-NB-5P samples display the absorption edges at the wavelength of 505 and 520 nm, respectively, because Ni_3B is black solid powders and has strong absorption in the visible region. After loaded Ni_3B cocatalyst, the sample of BVO-NB-5P exhibits a significantly higher light absorption ability than the pristine $BiVO_4$ film. This analysis demonstrates that the introduction of Ni_3B could distinctly enhance the optical response ability of BVO-NB-5P. Furthermore, the bandgap of $BiVO_4$ and BVO-NB-5P samples can be determined by Eq. (1)

$$(\alpha h\nu)^n = A(h\nu - E_g) \quad (1)$$

where α, h, ν, and A are absorption coefficients, Planck's constant, incident light frequency, and the proportionality constant, respectively. The E_g is the band gap energy and n is the characteristic integer, which depends on the characteristics of the optical transition in a semiconductor. $BiVO_4$ as a direct semiconductor so that the value of n is 2. Therefore, as shown in Fig. 7(b), the band gap energies of $BiVO_4$ and BVO-NB-5P samples are 2.49 and 2.44 eV, respectively. The reduced band gap value of BVO-NB-5P would be beneficial to the charge transfer and the utilization of solar energy.

The light absorption conversion efficiencies of $BiVO_4$ and BVO-NB-5P samples were calculated by Eq. (S4) in the ESM. As given in Fig. S2 in the ESM, both $BiVO_4$ and BVO-NB-5P display good light absorption conversion efficiencies in the absorption limit range. Meanwhile, the light absorption conversion efficiency of BVO-NB-5P is better than that of $BiVO_4$, which further indicates that the construction of composite system is beneficial to enhance the utilization efficiency of visible light.

To evaluate the photoelectrochemical performance of the samples, the LSV curves of $BiVO_4/Ni_3B$ photoelectrodes in 0.1 M Na_2SO_4 solution under AM 1.5 G light conditions are shown in Fig. 8(a). The photocurrent density of the samples increases with the increase of applied voltage. Compared with the pure $BiVO_4$ photoanode, the photocurrent density of the composite photoanode with surface modification of cocatalyst Ni_3B is significantly higher. However, due to the poor performance of amorphous Ni_3B, the photocurrent density of BVO-NB-5 is only slightly enhanced. And after annealing, the photocurrent density of BVO-NB-5 photoanode reached 1.01 mA·cm^{-2}, and then after pressing treatment, the photocurrent density of BVO-NB-5P photoanode is further increased to 1.47 mA·cm^{-2}, which is about 2.8 times that of pure $BiVO_4$. This result indicates that the loading Ni_3B cocatalyst can effectively improve the performance of $BiVO_4$ photoanode. Especially after the pressing treatment, the binding of $BiVO_4$ and Ni_3B is tighter, and the carrier transport rate on the surface can be further increased, thus obtaining a higher photocurrent density. In addition, compared to $BiVO_4$, the onset potentials (the voltage value when the photocurrent changes from negative to positive) of the BVO-NB-5 and BVO-NB-5P samples are negatively shifted by 0.02 and 0.14 V, respectively. The negative shift of the starting potential suggests that the BVO-NB-5P sample can greatly accelerate the transport and reaction of holes on the surface of the $BiVO_4$ photoanode. PEC performance of photoanodes with the Na_2SO_3 scavenger electrolyte displays in Figs. 8(b) and 8(c). The photocurrent densities are at 1.23 and 1.56 mA·cm^{-2} (1.23 V vs. RHE) for $BiVO_4$ and BVO-NB-5P, respectively. To further investigate the photoelectrochemical performance of $BiVO_4$ and composite photoanodes, the applied bias photoelectric conversion efficiency (ABPE) of each sample was calculated using Eq. (S1) in the ESM. From Fig. 8(d), the $BiVO_4$ photoanode exhibits the highest efficiency of 0.085% (0.93 V vs. RHE). Noticeably, the BVO-NB-5P sample shows the highest ABPE value with a conversion efficiency of 0.25% at 0.89 V vs. RHE, and the conversion efficiency of BVO-NB-5P is improved by about 1.94 times compared to the pure sample. Further, the charge separation efficiency ($\eta_{separation}$) and surface

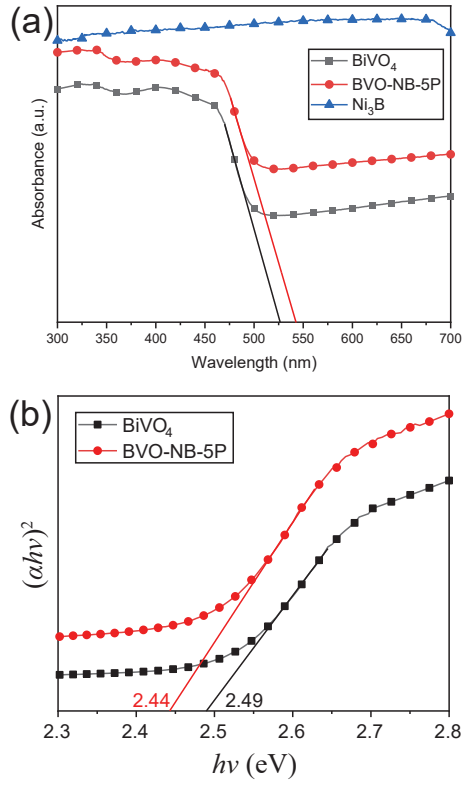

Figure 7 (a) The UV–vis diffuse reflectance spectra and (b) tauc plots of $BiVO_4$ and BVO-NB-5P.

charge injection efficiency ($\eta_{injection}$) caused by the decoration of Ni_3B on the $BiVO_4$ structure were investigated (Eqs. (S5) and (S6) in the ESM). And a hole-consuming agent (0.1 M Na_2SO_3) is used as the electrolyte. The sacrificial agent is considered to provide 100% of the surface catalytic efficiency, inferring that all the holes at the surface are consumed. The results are shown in Figs. 8(e) and 8(f), the $\eta_{separation}$ of BVO-NB-5P is not increased much after loaded cocatalyst Ni_3B. However, the $\eta_{injection}$ of BVO-NB-5P reaches approximately 94%, significantly higher than 31% of bare $BiVO_4$ at 1.23 V vs. RHE. The high value of $\eta_{injection}$ for BVO-NB-5P can be ascribed that the coating Ni_3B film greatly suppresses the surface recombination of the photogenerated holes, and increases the kinetics of oxygen evolution on the surface.

Figure S3 in the ESM shows the photocurrent density–time (*I*–*t*), LSV, EIS, and open-circuit photovoltage (OCP) performance of composite photoanode. It is worth noting that BVO-NB-5 shows the best PEC performance. In addition, Fig. 9(a) shows the *I*–*t* plots of the samples obtained at 0 V bias voltage. After simulated by one sun illumination, the transient photocurrent of all composited samples is better than that of the pristine $BiVO_4$. BVO-NB-5P exhibits the highest current due to its good combination under 20 N press. This phenomenon can be ascribed to the construction of close contacts between $BiVO_4$ and Ni_3B, which greatly suppresses the recombination efficiency of photo-induced holes and electrons. Figure 9(b) shows the photocurrent density versus potential of each sample under chopped illumination. Importantly, all samples display a fast photocurrent response, with BVO-NB-5P exhibiting the best performance with a photocurrent of 1.8 mA·cm^{-2} at 1.23 V. Compared to continuous light, chopped light conditions allow photogenerated carriers to be consumed under dark state conditions without aggregating on the catalyst surface, thus further increasing the photocurrent density. EIS plots was used to depict the resistance for charge transfer and separation of the electrode/electrolyte contact area at the solid–liquid interface (Fig. 9(c)). In general, the arc radius of the electrochemical impedance spectrum is proportional to the resistance of the sample. The smaller the arc radius, the stronger the transport capacity of the photogenerated electron–hole pair, i.e., the lower the resistance. As displayed in Fig. 9(c), much smaller arc radius of EIS is observed for composite photoelectrodes compared to pure $BiVO_4$, which indicates the resistance for charge transfer at the $Ni_3B/BiVO_4$/electrolyte interface is much smaller.

The OCP measurement was performed to investigate the PEC activity of samples. The photoanode under irradiation conditions undergoes charge separation and produces photoelectrons, which

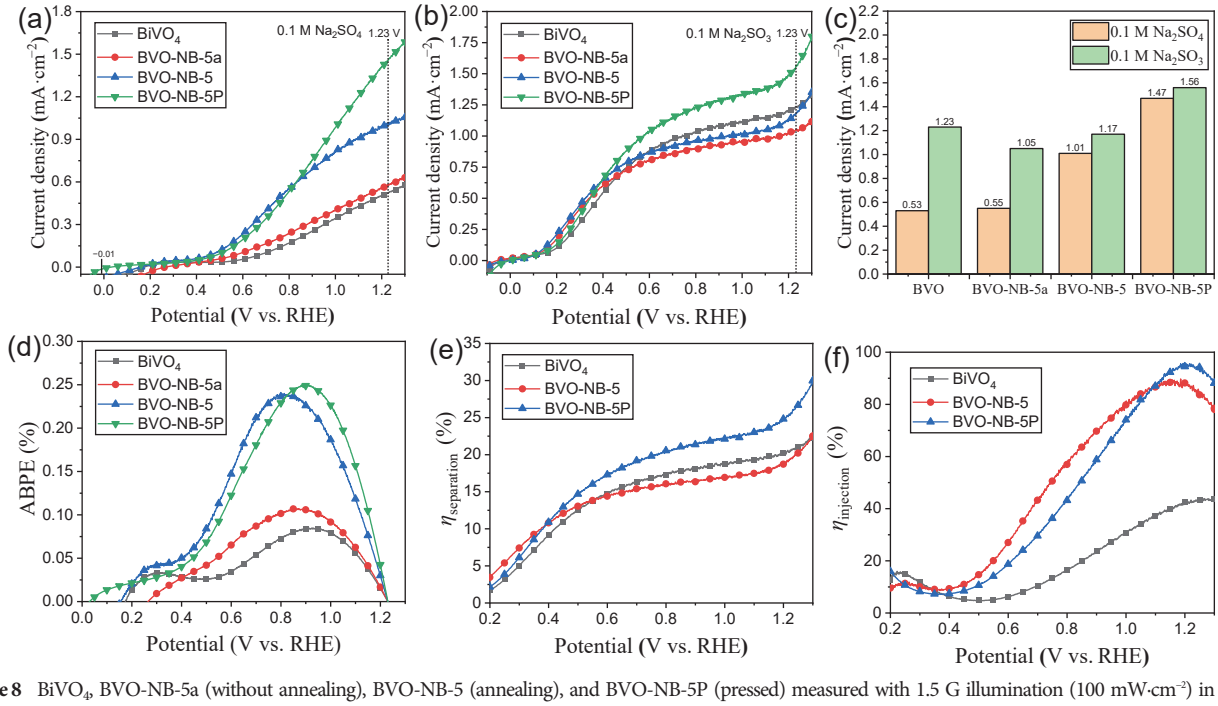

Figure 8 $BiVO_4$, BVO-NB-5a (without annealing), BVO-NB-5 (annealing), and BVO-NB-5P (pressed) measured with 1.5 G illumination (100 mW·cm^{-2}) in 0.1 M Na_2SO_4. (a) LSVs, (b) 0.1 M Na_2SO_3, (c) corresponding photocurrent density at 1.23 V vs. RHE, (d) applied bias photon-to-current efficiencies (ABPE) of the photoanodes, (e) calculated charge transport efficiency, and (f) charge injection efficiency.

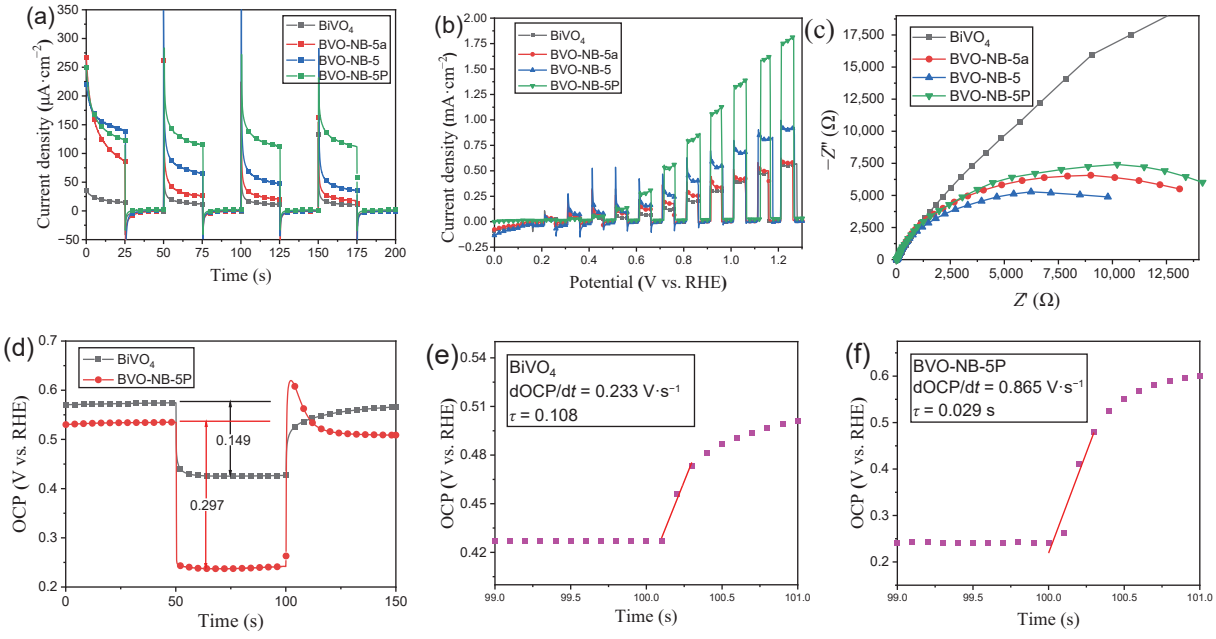

Figure 9 $BiVO_4$ and composite photoelectrodes. (a) *I*–*t* curves, (b) LSV curves under chopped illumination, (c) Nyquist plot, (d) open-circuit potential photovoltage (V_{oc}), and (e) and (f) carrier life-time.

can be illustrated by the transfer of OCP to negative values. As shown in Fig. 9(d), the OCP of BVO-NB-P and $BiVO_4$ is 0.297 and 0.149 V, respectively. This result indicates that BVO-NB-5P shows excellent photoelectrochemical properties. Moreover, Eq. (S7) in the ESM is used to calculate the carrier life-time of the samples, and the carrier decay life-time of $BiVO_4$ and BVO-NB-5P are 0.108 and 0.029 s, respectively (Figs. 9(e) and 9(f)). The greatly reduced life-time is induced by Ni_3B for carriers fast reaction, which significantly improves the reaction rate of oxygen evolution on the surface of BVO-NB-5P photoanode.

Mott–Schottky plots of $BiVO_4$ and BVO-NB-5P photoelectrodes were implemented at 500, 750, and 1,000 Hz, respectively, as displayed in Fig. 10. The negative slopes of $BiVO_4$ and BVO-NB-5P are corresponding to the n-type semiconductors. The flat-band potential (E_{fb}) exhibits a slightly negative shift for introduction of the Ni_3B cocatalyst, implying an increase of the band bending at the interface and smaller onset potential for PEC water oxidation.

To evaluate the water decomposition capability of the samples, both H_2 and O_2 evolution were detected at 1.23 V vs. RHE under AM 1.5 G (100 mW·cm^{-2}). As shown in Figs. 11(a) and 11(b), the gas evolution amounts increase linearly with reaction time. After 4 h illumination, the produced H_2 and O_2 amounts on the Pt and BVO-NB-5Pph-otoanode are 199 and 98.6 μmol, respectively, corresponding to the 2:1 ratio of the water splitting reaction. Moreover, the hydrogen production yield of BVO-NB-5P (50.9 μmol·h^{-1}·cm^{-2}) is 11.3 times higher than BiVO4 (4.5 μmol·h^{-1}·cm^{-2}). The results indicate that Ni_3B as cocatalyst is essential for improving carriers' oxidization reaction and solar conversion efficiency.

The proposed mechanism of BVO-NB-5P photoelectrode for water splitting is illustrated in Fig. 11(c). $BiVO_4$ produces electron–hole (e^-–h^+) pairs under light irradiation. Then the e^- in the CB entered the external circuit under applied bias to reduce the H^+ at the surface of the Pt cathode. Meanwhile, the photogenerated h^+ of $BiVO_4$ was transported to the cocatalyst Ni_3B to participate in the oxidized reaction of OH^- for evolution O_2. The Ni_3B as an efficient cocatalyst used in electrochemistry could also easily accelerate the OER of water splitting to improve the PEC performance.

4 Conclusions

A simple method to fabricate $BiVO_4$ photoelectrodes with inexpensive electrocatalytic Ni_3B cocatalyst was reported. Annealed Ni_3B can effectively reduce the water oxidation barrier between the $BiVO_4$ photoanode and electrolyte, resulting in a drastic increase in the photocurrent density. Interestingly, this work also emphasizes that the BVO-NB-5P sample after pressing exhibits the highest photocurrent density of 1.47 mA·cm^{-2} and hydrogen production yield of 50.9 μmol·h^{-1}·cm^{-2} at 1.23 V vs. RHE, which are 2.8 and 11.3 times of the PEC performance of pure $BiVO_4$, respectively. The spin coated $BiVO_4$/Ni_3B has a significant potential for solar-driven water splitting as a kind of sustainable, economical, and efficient photoelectrodes.

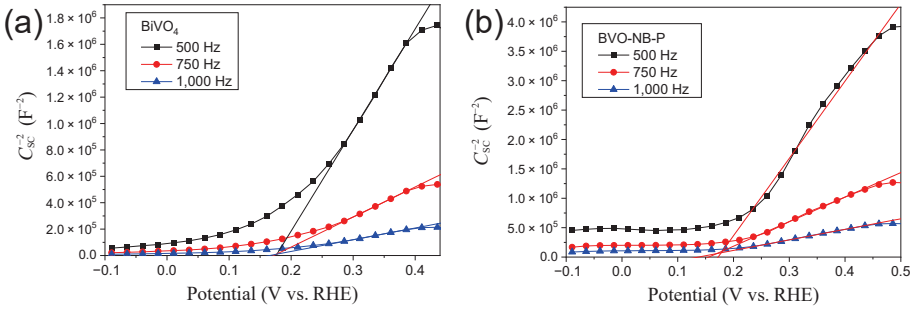

Figure 10 M–S curves of (a) $BiVO_4$ and (b) BVO-NB-P were measured at 500, 750, and 1,000 Hz, respectively.

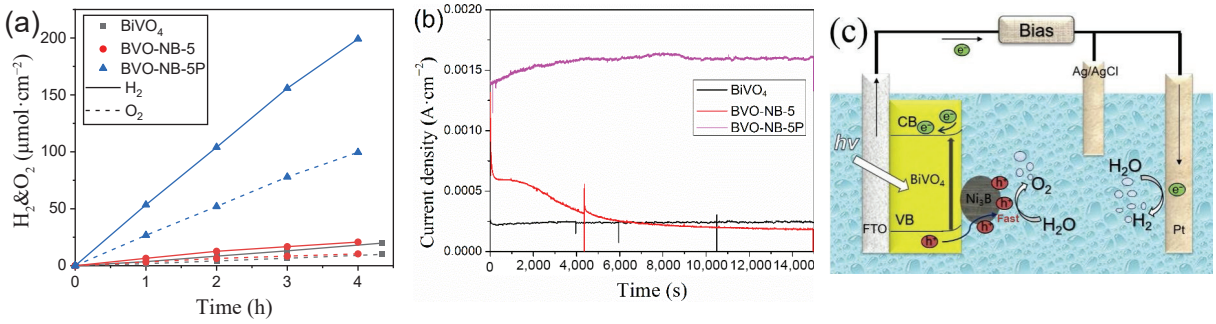

Figure 11 $BiVO_4$, BVO-NB-5, and BVO-NB-5P under AM 1.5 G and 1.23 V vs. RHE. (a) Production rates of H_2 and O_2, (b) stability test, and (c) schematic mechanism.

Acknowledgements

The financial support for this study by the Natural Science Foundation of Shandong Province (No. ZR2019EMQ001), Technology Project of Qingdao (No. 22-3-7-cspz-9-nsh), and the National Natural Science Foundation of China (No. 21476262) is gratefully acknowledged.

Electronic Supplementary Material: Supplementary material (XRD patterns, *I–t* curves, LSVs, Nyquist plot, and OCP versus time curve of samples) is available in the online version of this article at https://doi.org/10.1007/s12274-022-5079-7.

References

[1] Yu, L. Q.; Zhang, Y. P.; He, J. D.; Zhu, H. F.; Zhou, X. Y.; Li, M.; Yang, Q. L.; Xu, F. Enhanced photoelectrochemical properties of α-Fe_2O_3 nanoarrays for water splitting. *J. Alloys Compd.* **2018**, *753*, 601–606.

[2] Ye, S.; Ding, C. M.; Liu, M. Y.; Wang, A. Q.; Huang, Q. G.; Li, C. Water oxidation catalysts for artificial photosynthesis. *Adv. Mater.* **2019**, *31*, 1902069.

[3] Yu, Z. Y.; Duan, Y.; Feng, X. Y.; Yu, X. X.; Gao, M. R.; Yu, S. H. Clean and affordable hydrogen fuel from alkaline water splitting: Past, recent progress, and future prospects. *Adv. Mater.* **2021**, *33*, 2007100.

[4] Zhang, Y. P.; He, J. D.; Yang, Q. L.; Zhu, H. F.; Wang, Q. Q.; Xue, Q. Z.; Yu, L. Q. Solution quenched *in-situ* growth of hierarchical flower-like $NiFe_2O_4/Fe_2O_3$ heterojunction for wide-range light absorption. *J. Power Sources* **2019**, *440*, 227120.

[5] Duan, L. J.; Zhu, H. F.; He, J. D.; Yang, Q. L.; Zhao, X. Y.; Zhang, Y. P.; Yu, L. Q. Oriented titania nanotube biphase junction arrays on water splitting. *Mater. Sci. Semicond. Process.* **2021**, *126*, 105667.

[6] Fujishima, A.; Honda, K. Electrochemical photolysis of water at a semiconductor electrode. *Nature* **1972**, *238*, 37–38.

[7] Hisatomi, T.; Kubota, J.; Domen, K. Recent advances in semiconductors for photocatalytic and photoelectrochemical water splitting. *Chem. Soc. Rev.* **2014**, *43*, 7520–7535.

[8] Li, K. X.; Feng, D. M.; Tong, Y. Hierarchical metal sulfides heterostructure as superior bifunctional electrode for overall water splitting. *ChemSusChem* **2022**, *15*, e202200590.

[9] Lu, Y.; Yang, Y. L.; Fan, X. Y.; Li, Y. Q.; Zhou, D. H.; Cai, B.; Wang, L. Y.; Fan, K.; Zhang, K. Boosting charge transport in $BiVO_4$ photoanode for solar water oxidation. *Adv. Mater.* **2022**, *34*, 2108178.

[10] Malathi, A.; Madhavan, J.; Ashokkumar, M.; Arunachalam, P. A review on $BiVO_4$ photocatalyst: Activity enhancement methods for solar photocatalytic applications. *Appl. Catal. A: Gen.* **2018**, *555*, 47–74.

[11] Wang, S. C.; He, T. W.; Chen, P.; Du, A. J.; Ostrikov, K.; Huang, W.; Wang, L. Z. *In situ* formation of oxygen vacancies achieving near-complete charge separation in planar $BiVO_4$ photoanodes. *Adv. Mater.* **2020**, *32*, 2001385.

[12] Tan, H. L.; Amal, R.; Ng, Y. H. Alternative strategies in improving the photocatalytic and photoelectrochemical activities of visible light-driven $BiVO_4$: A review. *J. Mater. Chem. A* **2017**, *5*, 16498–16521.

[13] Zhou, Z. M.; Chen, J. J.; Wang, Q. L.; Jiang, X. X.; Shen, Y. Enhanced photoelectrochemical water splitting using a cobalt-sulfide-decorated $BiVO_4$ photoanode. *Chin. J. Catal.* **2022**, *43*, 433–441.

[14] Wang, S. C.; Liu, B. Y.; Wang, X.; Zhang, Y. J.; Huang, W. Nanoporous $MoO_{3-x}/BiVO_4$ photoanodes promoting charge separation for efficient photoelectrochemical water splitting. *Nano Res.* **2022**, *15*, 7026–7033.

[15] Wang, L.; Su, J. Z.; Guo, L. J. Hierarchical growth of a novel Mn-Bi coupled $BiVO_4$ arrays for enhanced photoelectrochemical water splitting. *Nano Res.* **2019**, *12*, 575–580.

[16] Hu, K. K.; E, L.; Li, Y. J.; Zhao, X. Y.; Zhao, D.; Zhao, W.; Rong, H. Photocatalytic degradation mechanism of the visible-light responsive $BiVO_4/TiO_2$ core–shell heterojunction photocatalyst. *J. Inorg. Organomet. Polym. Mater.* **2020**, *30*, 775–788.

[17] Yin, X.; Liu, Q.; Yang, Y. H.; Liu, Y.; Wang, K. K.; Li, Y. M.; Li, D. W.; Qiu, X. Q.; Li, W. Z.; Li, J. An efficient tandem photoelectrochemical cell composed of $FeOOH/TiO_2/BiVO_4$ and Cu_2O for self-driven solar water splitting. *Int. J. Hydrogen Energy* **2019**, *44*, 594–604.

[18] Coelho, D.; Gaudêncio, J. P. R. S.; Carminati, S. A.; Ribeiro, F. W. P.; Nogueira, A. F.; Mascaro, L. H. Bi electrodeposition on WO_3 photoanode to improve the photoactivity of the $WO_3/BiVO_4$ heterostructure to water splitting. *Chem. Eng. J.* **2020**, *399*, 125836.

[19] Reddy, C. V.; Reddy, I. N.; Koutavarapu, R.; Reddy, K. R.; Kim, D.; Shim, J. Novel $BiVO_4$ nanostructures for environmental remediation, enhanced photoelectrocatalytic water oxidation and electrochemical energy storage performance. *Sol. Energy* **2020**, *207*, 441–449.

[20] Kang, Z. H.; Lv, X. D.; Sun, Z.; Wang, S. Q.; Zheng, Y. Z.; Tao, X. Borate and iron hydroxide co-modified $BiVO_4$ photoanodes for high-performance photoelectrochemical water oxidation. *Chem. Eng. J.* **2021**, *421*, 129819.

[21] González, D.; Sodupe, M.; Rodríguez-Santiago, L.; Solans-Monfort, X. Metal coordination determines the catalytic activity of IrO_2 nanoparticles for the oxygen evolution reaction. *J. Catal.* **2022**, *412*, 78–86.

[22] Chen, H.; Zou, X. X. Intermetallic borides: Structures, synthesis and applications in electrocatalysis. *Inorg. Chem. Front.* **2020**, *7*, 2248–2264.

[23] Gupta, S.; Patel, M. K.; Miotello, A.; Patel, N. Metal boride-based catalysts for electrochemical water-splitting: A review. *Adv. Funct. Mater.* **2020**, *30*, 1906481.

[24] Arivu, M.; Masud, J.; Umapathi, S.; Nath, M. Facile synthesis of Ni_3B/rGO nanocomposite as an efficient electrocatalyst for the oxygen evolution reaction in alkaline media. *Electrochem. Commun.* **2018**, *86*, 121–125.

[25] Wu, Y. Y.; Yin, J. Q.; Jiang, W.; Li, H. J.; Liu, C. B.; Che, G. B. Constructing urchin-like Ni_3S_2@Ni_3B on Ni plate as a highly efficient bifunctional electrocatalyst for water splitting reaction. *Nanoscale* **2021**, *13*, 17953–17960.